Titanium Nanoparticle Regulates Innate Immunity

Jacob J. Whittaker,[a,#,*] David Eikrem,[b,#] Joanna Whittaker,[c] Gulaim A. Seisenbaeva,[a] Karin Fromell,[b] Kristina N. Ekdahl,[b,d] Bo Nilsson,[b] Mats Sandgren,[a] and Vadim G. Kessler[a]

[a] Department of Molecular Sciences, Swedish University of Agricultural Sciences, Uppsala, Sweden.

[b] Department of Immunology, Genetics and Pathology, Rudbeck Laboratory C5:3, Uppsala University, SE-751 85 Uppsala, Sweden.

[c] Department of Chemistry, BMC, Uppsala University, Sweden

[d] Linnæus Centre for Biomaterials Chemistry, Linnæus University, SE-391 82 Kalmar, Sweden

[#] Authors contributed equally

[*] Correspondence should be addressed to Jacob Whittaker (Jacob.whittaker@slu.se)

Abstract

In-vivo studies on wound healing have shown that small metal oxide nanoparticles (NPs), such as titania, ferria, and alumina, promote wound closure, likely by enhancing blood coagulation and via activation of the contact system. However, titania differs from the others as it supports the regrowth of normal skin tissue without scarring. This unique effect was hypothesised to result from its ability to suppress inflammation, possibly by interfering with the complement system. E*x-vivo* whole blood experiments within the present study confirm that titania NPs significantly dampen the immune response and surface plasmon resonance (SPR) biosensor analysis confirms that the nanoparticle binds with nanomolar affinity to complement C3, a central protein in the human innate immune system. To elucidate the molecular basis of this effect, we developed a novel cryo-electron microscopy (cryo-EM) methodology capable of resolving the challenging interface between metal NPs and proteins. This approach revealed that TiO□ binds with high specificity to a single domain on C3. The NP restricts the conformational dynamics of C3 and thus blocks the initiation of the complement cascade. These structural and biophysical insights support the biochemical findings and previous observations within the contact system. Our method advancement demonstrates that cryo-EM can uncover physiologically relevant interactions between proteins and nanomaterials at high resolution and offers a strong foundation for others investigating metal-biological interactions.

Introduction

Engineered nanoparticles, such as silver, gold, zinc and titanium oxides, are products of modern science and have only been introduced into the environment within the last few decades. In particular, titanium dioxide (TiO_2) nanoparticles have seen usage in an immense range of everyday products such as a whitening food additive (E171), confectionary, paint, hygiene and personal care products.[1-4] Synthesised TiO_2 nanoparticles can range from one nanometre in diameter through to several hundred nanometres, with each size class capable of eliciting distinct biological responses.[5] Notably, macro-scale titania from implanted surfaces or environmental exposure can be gradually etched away by bodily fluids into smaller nanoparticle oxides, potentially contributing to systemic nanoparticle exposure.[6-8] Despite the recent increase in anthropogenic metal-based nanoparticles and increased daily exposure, very limited safety information is available concerning their biological effect.[9] Toxicity considerations are particularly relevant for TiO_2 nanoparticles that are <5 nm in diameter due to their ability to cross the blood-brain barrier and penetrate cellular walls,[10, 11] causing protein misfolding, enzymatic inhibition, dysregulation, aggregation and structural alteration.[12-15] Previous work from our groups have unambiguously shown that a titanium nanoparticle 3.5 nm in diameter, in fact, improves burn wound healing and skin tissue regeneration in the contact activation system via upregulation (Figure 1).[16]

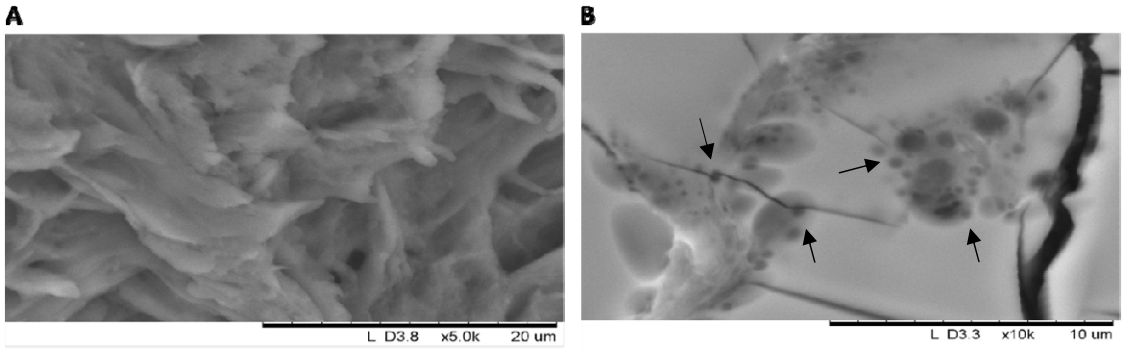

Figure 1. Comparative SEM images showing the influence that titanium nanoparticles have on human skin samples. **A**) Untreated human skin sample in the process of healing following trauma. **B**) Human skin sample coated with TiO_2 nanoparticle.[16]

Throughout *in-vivo* studies in rats using these nanoparticles, we were able to enhance wound healing to such an extent that the regeneration of skin resulted in nearly no scar tissue. Using scanning electron microscopy (SEM), comparisons between naturally-healing skin and nanoparticle-

54 coated human skin showed remarkable differences in the skin surface morphologies. Naturally-
55 healing skin exhibited a randomly dispersed, fibrous surface, whereas skin coated with TiO_2
56 appeared as smooth and well-organised with minimal evidence of trauma. Importantly, compared to
57 the untreated control, there was a significantly quicker reduction of inflammation at the wound
58 site. Other metal oxide nanoparticles were also tested, but none were able to elicit the same
59 beneficial results as observed for titania. As the contact activation system operates together with
60 other regulatory systems, we wanted to gain a molecular-level understanding into what was causing
61 these nanoparticles to impart such considerable effects. This led us to begin investigating their
62 influence on the complement system, a very closely-linked immune regulatory system.[17, 18]
63 Over the course of 500 million years, the complement system in vertebrates has evolved into the
64 highly advanced and intricate defence mechanism found in humans today. This system involves the
65 coordination of ~50 different immune regulation factors and proteins.[19-21] The complement system
66 functions in tissue, plasma, intracellularly and demonstrates exceptional sensitivity to antibodies,
67 foreign microbial sugars and pathogens.[22] The C3 zymogen, an inactive enzyme precursor that
68 requires activation to function, is perhaps the most significant protein in the entire complement
69 cascade. It exists as the most abundant complement protein found in the blood of healthy humans
70 at concentrations above 1.2 mg/mL.[23] For activation of C3 to occur, a small 9 kDa domain (C3a)
71 must be cleaved from the main 176 kDa chain (C3b) by a C3 convertase or serine proteases.[24-26] This
72 promotes a significant conformational shift of C3b and the exposure of a highly reactive thioester
73 which is responsible for the opsonisation (tagging) of foreign particles for destruction by
74 downstream immune system machinery.[27] Importantly, dysregulation or dysfunction of C3 has been
75 closely linked to diseases such as lupus and meningococcal meningitis, making it a clinically
76 significant target for both understanding immune pathology and developing new treatments.[28-30]
77
78 Here we present the first biochemical and structural evidence of a physiological TiO_2 nanoparticle
79 downregulating the functional activity of wild-type human complement C3. Haemolysis results from
80 whole blood models show that tiny quantities of TiO_2 are enough to significantly decrease the
81 activity of C3 and act as an alternative pathway-specific inhibitor. Furthermore, surface plasmon
82 resonance (SPR) biosensor analysis shows that the NP has a remarkably strong affinity for C3. The K_D
83 value of 24 nM is six-times lower than that estimated for the original C3 commercial inhibitor,

84 Compstatin Cp01.[31, 32] Structurally, a major challenge in modern microscopy is the inability to
85 visualise samples of mixed organic-inorganic species. We have overcome this obstacle and
86 developed a methodology which has enabled us to observe this exciting interaction at viable
87 resolutions for retaining molecular-level information. Our single-particle cryo-EM studies reveal a
88 strong and specific interaction between a single TiO_2 nanoparticle and protein domain is enough to
89 deactivate the immune functionality of C3. The location of the bound nanoparticle restricts the
90 motion of C3 and inhibits the formation of protein-protein interactions necessary for continued
91 immune function. Our findings represent an important step towards enabling cryo-EM as a tool
92 capable of capturing the communication between physiological proteins and interacting inorganic
93 species. On one hand, we have provided valuable insight into how these physiologically-active TiO_2
94 nanoparticles promote wound healing, while on the other hand, these effects are uncovered with
95 molecular-level detail.
96
97
98

99 Results

100 Full-range of C3 flexibility revealed

101 The most compact state, shown in Figure 2a, appears as the dominant species in solution and
102 represents the inactive state conformation. This arrangement shows the thioester domain (TED)
103 compressed and adjacent to the macroglobulin ring (MG) domains of MG2 and MG6. The 120 Å
104 diameter of this compressed structure supports the biophysical results and explains our observed
105 discrepancy with previous structures (see ESI). The interactions between the TED and MG domains
106 are facilitated mainly through dipole contacts rather than strong ionic interactions. This feature
107 allows for the movement experienced by the MG domains to proceed freely. In fact, of the three
108 interacting domains in this region, there are almost no electrostatic interactions or hydrogen bonds
109 formed. Instead, a select few complementary hydrophobic and hydrophilic pockets of amino acids
110 are enough to stabilise this conformation (Figure 3).

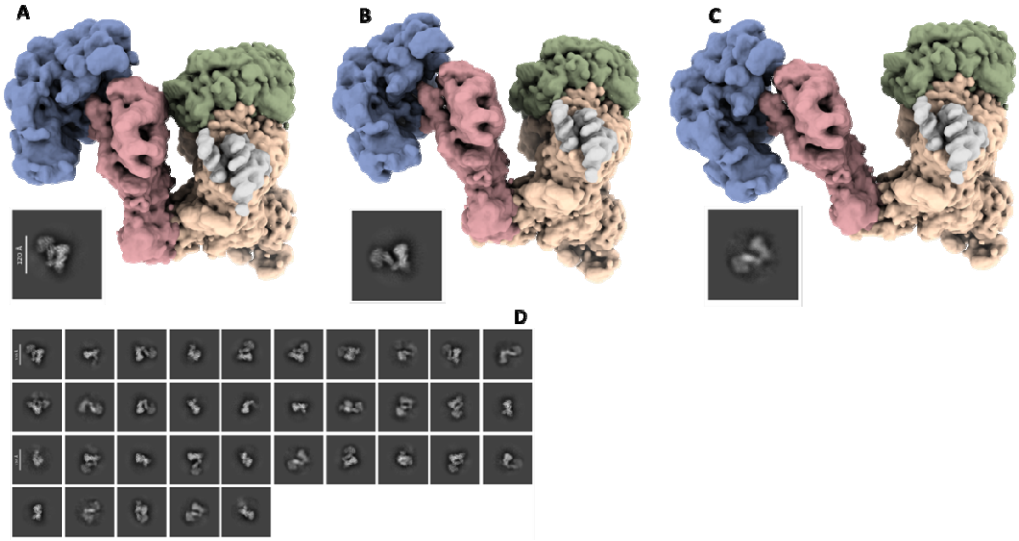

Figure 2. Cryo-EM densities and 2D classes showing the flexible heterogeneity of native C3 in a sample. The protein density is coloured to show the functional areas, such as C3a (grey), TED (green), connecting arm (red), MG head (blue) and body regions (beige). **A)** The most compressed, inactive conformation. **B)** An intermediate state exposing a gap between the central arm and TED regions. **C)** The extended state of C3 where the connecting arm region has moved away from the biologically-active TED, exposing it to potential foreign particles. **D)** 2D classes which exemplify the large conformational range achieved by C3.

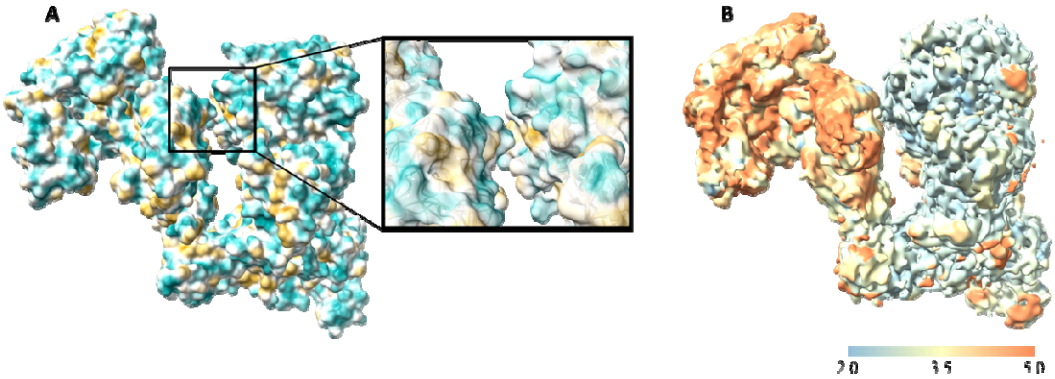

Figure 3. **A)** Native C3 electron density displayed as a hydrophobic (yellow) and hydrophilic (cyan) map with a close-up view of the interacting regions between the connecting arm and thioester domain. **B)** The local resolution electron map of native C3 calculated to $FSC_{0.143}$.

3D Flexibility analysis shows two distinct states attributed to MG ring domains 1 - 6 which possess the ability to locally swivel and pivot in-place (ESI Figure S2). This was an unexpected finding, as the structurally well-characterised macroglobulin ring domain is reported as rigid.[33, 34] Combining both 3D variability and 3D flexibility analyses, the global hinge-like motion between the contracted

128 and expanded states could be resolved in addition to the flexible local motions experienced by
129 each domain throughout the full movement. The MG domain movement between each
130 conformational endpoint was found to reach up to 28 Å, with the MG2 and MG6 connecting arm
131 region shifting by 12 Å. Minor classes found in 2D classification suggest that the extension may
132 actually be greater than this, however these views were too rare to be reliably incorporated into
133 the 3D variability constructions. In biological systems, the thioester domain acts as a "warhead" to
134 connect to the detected foreign particle. The current structural series shows the MG2 and MG6
135 domains assist with this tagging process by uncovering the thioester region and exposing it for
136 binding. These domains act as an extending arm which moves the bulky MG regions away from the
137 TED by roughly 30°. Furthermore, the MG7 domain exhibits a slight bending motion which affords
138 more solvent-accessible space for the linker domain to extend into.
139
140 Each "compact" and "stretched" conformation could be reconstructed to a $FSC_{0.143}$ of 3.0 Å and 4.0
141 Å, respectively (ESI Supplementary Table 1). The local resolution range varied more depending on
142 the degree of flexibility demonstrated in each conformational state. The alpha chain of C3
143 remained rigid with local resolution reconstructions of 2.5 Å possible. The flexible MG ring domains
144 could be reconstructed to approximately 5 Å in the extended pose while a higher resolution of 3.2 Å
145 was achievable in the contracted, more rigid conformation.
146

147 TiO_2 nanoparticle and human complement C3 interact with nanomolar affinity

148 Repeating the DLS and thermal unfolding experiments on TiO_2 in the same buffered system as C3
149 proved unsuccessful as the presence of salt promoted the near-immediate aggregation and gelation
150 of the nanoparticle colloid throughout a range of concentrations (ESI Figure S3a). Instead using only
151 filtered water, the nanoparticles showed no signs of aggregation which was confirmed by DLS as the
152 TiO_2 particles were found to be of a homogenous diameter and stable at room temperature for 2
153 hours (ESI Figure S3b). After confirming that C3 was stable in filtered water, several concentrations
154 of TiO_2 nanoparticle were added to differing aliquots of 0.4 mg/mL C3 for DLS and nanoDSF analysis
155 (ESI Figure S3c). DLS results showed no appreciable indications of protein or nanoparticle
156 aggregation. NanoDSF showed near identical T_m inflection points for C3 in both water and buffered
157 solution over a range of temperatures. Importantly, the addition of TiO_2 resulted in an increase of

158 T_m by ~7 for several separate concentrations of nanoparticle, demonstrating a meaningful
159 interaction and significant thermostabilising effect of the TiO_2 species on C3.
160
161 Importantly, the interaction between the two species was confirmed and characterised via SPR
162 biosensor analysis. The affinity between the nanoparticles and the C3 protein was high, as
163 indicated by the estimated K_D of 24 nM (Figure 4). The poor fit using a 1:1 interaction model (Figure
164 4A) suggested a more complex binding event than a simple Langmuir interaction (i.e. a 1-step
165 reversible interaction with a 1:1 stoichiometry). The improved fit using a two-state reaction (Figure
166 4B) supports an interaction involving a conformational change of the protein upon binding of the
167 NP. Given the conformationally-heterogenous tendency of C3, it is unsurprising that the SPR
168 biosensor data are consistent with ligand-induced conformational changes.[35] This direct and time-
169 resolved interaction mechanistic information therefore both supports the structural data, and
170 reveals that the interaction has a higher affinity than Compstatin Cp01 (150 nM), the original
171 commercial C3 inhibitor.

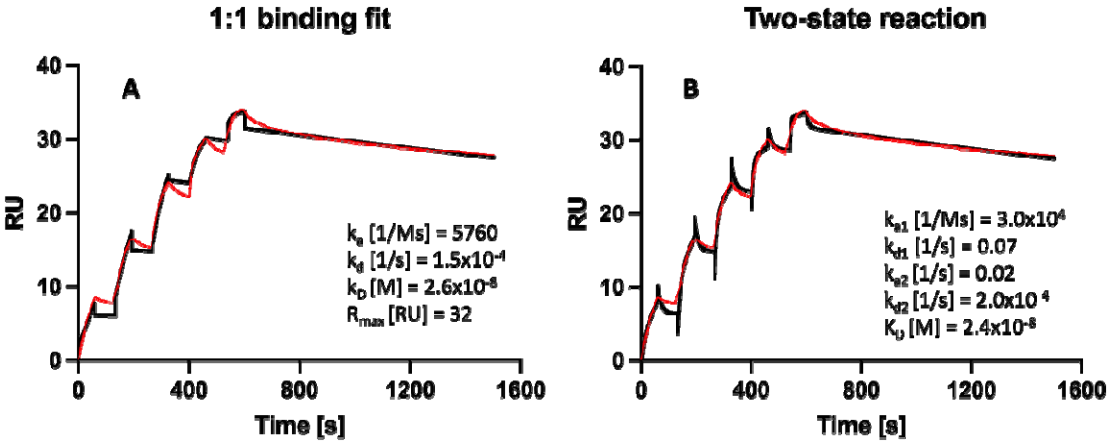

172
173 **Figure 4**. Sensorgrams of C3 interacting with immobilised TiO□ nanoparticles. Experimental traces from single cycle kinetic
174 experiments are in red, theoretical traces from global, non-linear regression analysis fitting are shown in black. The
175 sensorgrams represent a two-fold dilution series, starting from 10 μM down to 0.625 μM concentration. **A)** The theoretical fit
176 and kinetic parameters obtained by a global non-linear regression using a 1:1 interaction model. **B)** The sensorgram fitting
177 based on a two-state reaction model.
178

179 ## Biochemical assays show TiO_2 nanoparticle downregulates C3 activity

180 To test the effect TiO_2 may have on C3 function, the formation of the alternative pathway (AP)
181 convertase, C3bBb was considered. In the presence of Mg^{2+} ions, factor B (FB) binds to C3b forming
182 the foundation of an AP convertase, allowing for the action of factor D (FD) to cleave FB into
183 fragments Ba and Bb. In turn, C3bBb is formed with a substrate specificity for native C3, the
184 convertase cleaves off C3a generating C3b. Using C3b as a positive control, native C3 (1 μM) was
185 incubated with and without TiO_2 (1 μM) prior to the addition of FB and FD, relying on C3(H_2O)
186 contamination or spontaneous hydrolysis occurrence to enable convertase formation and Bb
187 generation. To analyse the effect of TiO_2, the ability for FB binding to native C3 was assessed by
188 comparing peak area values of FB and fragment Bb generation detected by a monoclonal antibody
189 against Factor Bb neoepitopes. The capillary electrophoresis data generated combined area for
190 Factor B and Factor Bb that were converted to percentage area in the Compass for Simple Western
191 (v 6.1.0) programme after peak naming. Figure 5A conveys the percent of Factor B remaining,
192 indicating a reduction in the AP convertase formation and activity, reducing Factor Bb generation.
193 In the presence of TiO_2, after 5 minutes, 95.1% FB remains (Native C3; 71.8%, C3b; 64.3%), 30
194 minutes 69.6% remains (Native C3; 13.9%, C3b; 15.6%) and 60 minutes 18.5% remains (Native C3;
195 11.9%, C3b; 8.9%).

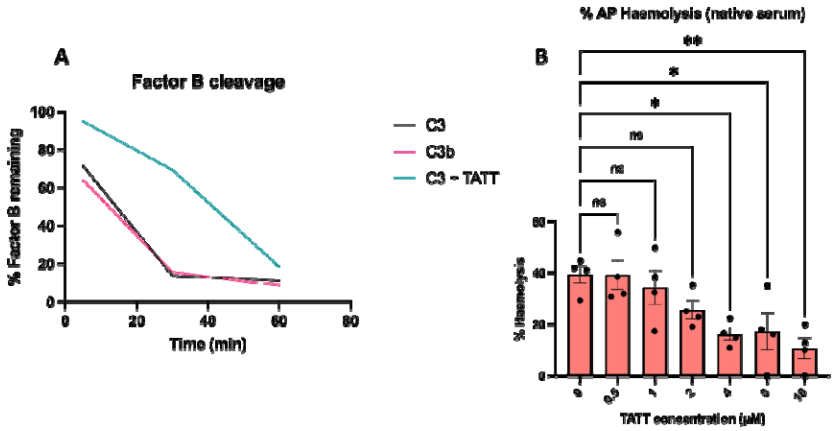

196

197 **Figure 5**. **A**) The percentage of factor B remaining after incubation of C3, C3b and C3 incubated with titania nanoparticles
198 over time calculated from the representative Wes immunoassay. Percent calculated from peak areas across factor B and Bb
199 populations in Compass for Simple Western software. **B**) Alternative pathway haemolysis assay of rabbit RBCs incubated with
200 C3 and increasing TiO_2 concentration. Measured at 540 nm and presented as an overall percentage of native serum. n=4,
201 data presented as mean ± SEM, significance presented as $^*P < 0.0332$ and $P^{**} < 0.0021$ determined by One-Way ANOVA with
202 Dunnet multiple comparison.

203 Haemolysis of red blood cells by C3 is inhibited with TiO_2

204 Building on the AP inhibition, the capacity for native C3 to maintain its haemolytic properties was
205 tested. Native C3 was incubated with incrementally increasing concentrations of TiO_2 (0.5, 1, 2, 4,
206 8 and 16 μM). Rabbit red blood cells (RBCs) were used in this experiment as they fail to inhibit
207 human complement and therefore become rapidly opsonised with C3b, enabling AP convertase and
208 subsequent membrane attack complex formation (MAC) assembly, leading to haemolysis. In this
209 serum dependant assay, an absorbance at 540 nm was recorded from native serum (total lysis), C3
210 depleted serum (blank) and the test samples of C3 with or without nanoparticles. The test samples
211 are reported as a percentage of total haemolysis and show a significant reduction in haemolysis as
212 nanoparticle concentration increases compared to neat native C3 (4 μM TiO_2 p= 0.0187; 8 μM TiO_2
213 p= 0.0268; 16μM TiO_2 p= 0.003) as shown in Figure 5B.
214

215 ## Direct observation of TiO_2 nanoparticles interacting with human C3

216 Using these optimal conditions, C3 and TiO_2 at differing ratios were applied to Quantifoil EM grids
217 and plunge frozen in liquid ethane in preparation for cryo-EM. Despite their modest size of 3.5 nm
218 and each nanoparticle possessing ~1800 titanium atoms, the nanoparticles were readily visible as
219 intense white spots on the micrograph with the 185 kDa protein in close proximity, barely visible as
220 a blurred grey signal (ESI Figure S4a). Additional sample processing in RELION 5.0 provided more
221 discernible particles of both C3 protein, TiO_2 nanoparticles as well as classes which showed both in
222 close proximity (ESI Figure S4b, S4d). Several ATLAS and eucentric height scans on different grids
223 suggested that both particle distribution and contrast were favourable in thicker ice. It was
224 immediately obvious from the micrographs that the nanoparticles further contributed to sample
225 heterogeneity as they did not appear to interact with the protein in a uniform manner. This became
226 evident from particle picking and 2D classification as several potential classes showed up to 3
227 nanoparticles may be interacting with a single protein, although at low alignment resolutions, this
228 may be attributed to increased particle densities in the thick ice regions. Using a non-standard
229 processing strategy in RELION 5.0 (see methods), we obtained a low-resolution electron density
230 map suitable for protein and nanoparticle fitting.
231

232 Despite a loss of resolution, the C3 core particle density which comprised of the thioester and
233 surrounding domains, matched very well with the previously-collected apo-C3 (amino acids ~550-

234 1641). Similarly to apo-C3, the macroglobulin ring density remained challenging to capture,
235 however the location of the missing domains could be approximated as the MG2 and MG6 domain
236 densities connecting the TED and MG ring, could be accounted for. The predominant pose of the C3
237 protein appears to be in the most compressed state, where the MG2 and MG6 domains rest directly
238 parallel to the thioester domain. Several charged residues along the linker region form
239 complementary interactions between oppositely charged residues on the external face of the
240 thioester domain, further stabilising this conformation (Figure 6A, B). The vast majority of 2D
241 classes also support this as we were unable to locate any rare views of extended protein in close
242 proximity to nanoparticle density. In fact, it seems as though these extended forms of C3 are only
243 observable in the absence of TiO_2.
244

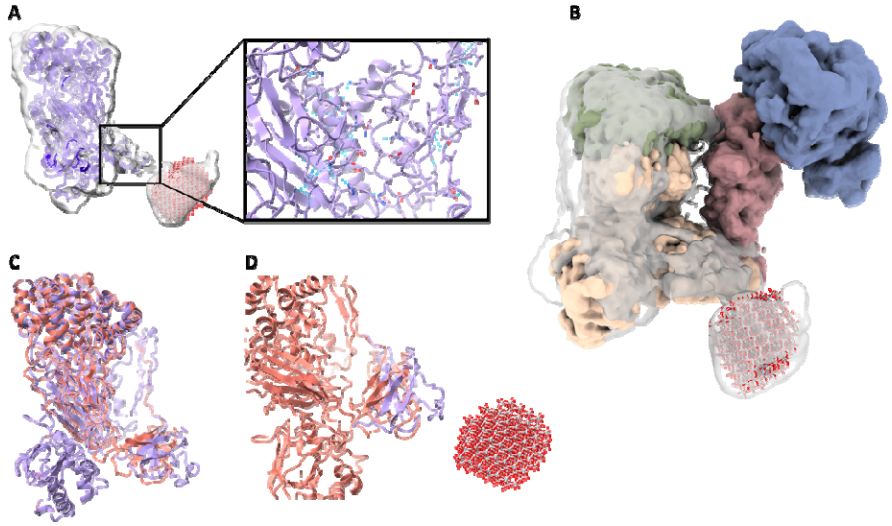

245
246 **Figure 6**. **A)** Electron density of the C3 core particle domains and the density attributed to the TiO_2 nanoparticle. Top right:
247 Intra-domain stabilising interactions between the linker and thioester domains. **B)** Overlaid electron density maps of the
248 native C3 and TiO_2-bound C3 structures highlighting the clear new density from the nanoparticle. **C)** Superimposed models of
249 reported C3 (orange) and C3 from the current work (violet), demonstrating the disparity between the MG7 domain locations
250 - RMSD 4.27 Å. **D)** Zoomed in image of the MG7 domains and the MG7 translated motion towards the TiO_2 nanoparticle.
251

252 Although lacking a defined binding site, protein flexibility and alignment challenges from spurious
253 classes, a clear density corresponding to the diameter of TiO_2 was located adjacent to the C3
254 electron density. Owing to the signal thresholding during data processing, the most intense signal
255 from the interior of the nanoparticle has been eliminated, leaving just the periphery which resulted
256 in a density with a hollow interior. The pseudo-spherical density can be confidently attributed to

257 the nanoparticle rather than the missing macroglobulin ring domains as the TiO_2 density not only
258 appears as the most intense after map contouring compared to protein signal, but is approximately
259 40 Å from the expected location of the macroglobulin ring. Furthermore, this region is situated well
260 outside the latent axis of motion displayed by the apo-C3 structure. Overlaying the reported
261 inactive structure with the nanoparticle-bound C3 shows that the majority of the structure is
262 unchanged, however producing a calculated RMSD of 4.27 Å relative to the MG7 domains of the
263 native and TiO_2 structures (Figure 7A, B). This variability is largely due to the apparent outward
264 shift of the MG7 domain (residues 807-911), as the RMSD of the remaining protein is 0.912 Å.

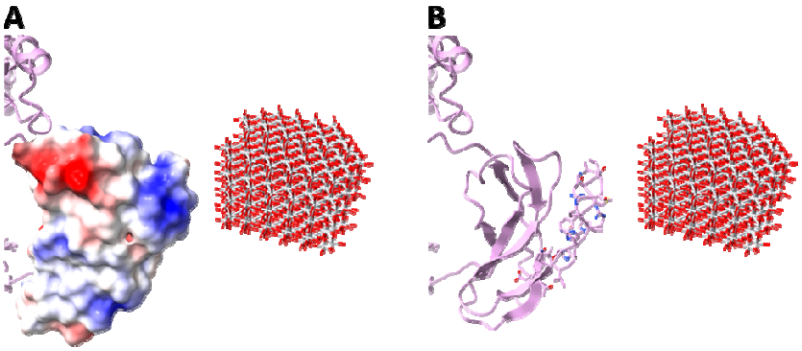

265

266 **Figure 7**. **A)** The electrostatic maps of MG7. Blue represents positively-charged domains, negatively-charged regions are
267 shown as red. **B)** Stick representation of the interacting residues in MG7 with TiO_2.

268

269 This macroglobulin domain is connected by two linker regions and is reported to move during
270 activation of C3, demonstrating a rotation of approximately 35 . This movement is facilitated by
271 the excision of the polypeptide chain between MG7 and MG8 by factor I, thus allowing the two MG
272 domains to nearly exchange positions.[36] Within an inactive C3, this domain is situated between the
273 linker and thioester domains, and has already been shown to move within the inactive state in the
274 apo-C3 structure. The location of MG7 in the current structure shows an outward shift of
275 approximately 9 Å in the opposing direction to MG8. As the linkers are still intact, a slight rotation
276 of this domain is afforded to form an interaction with the nanoparticle which is positioned 6 Å
277 adjacent to this domain. Given the significant electronegative nanoparticle, it was anticipated that
278 any interaction formed between the species would occur at an acidic or phosphorylated region of
279 the protein. A close inspection of the solvent-accessible residues on MG7 indeed confirm that the
280 nanoparticle likely participates in an outer-sphere complexation with several electropositive

281 residues (His846, Lys857, Arg858, Arg859, His860) in addition to hydrogen bonding interactions with
282 several more residues (Cys851, Thr855, Thr856, Gln862) within the region.
283

284 Discussion

285 Physiological impact of titanium nanoparticles in the complement system

286 Titania surfaces have proven to be incredibly useful, particularly within medical devices and
287 surgical implants, yet recent evidence shows that small (<10 nm) nanoparticles can be leached by
288 the blood from these bulk surfaces. To the best of our knowledge, our work represents original
289 insights into the physiological effects of small TiO_2 nanoparticles on our immune system, following
290 leaching from implanted surfaces. Significant improvements in the physical properties of
291 complement C3 with TiO□ indicated direct communication between the species at a range of
292 concentrations. This was surprising as neither of these components had any engineered binding
293 sites specific for the other. Furthermore, such an interaction was unable to be repeated for the
294 other complement proteins of C3a, factor B and factor D, in the alternative pathway, thus
295 suggesting that there was an element of protein selectivity. Confirmation of C3-TiO_2 specificity was
296 quantified by SPR biosensor analysis. The two-state reaction model provided a better fit to the
297 experimental data than the simple 1:1 interaction model, although both yielded essentially the
298 same K_D value. The improved fit obtained with the two-state model indicates that the binding is not
299 limited to a simple bimolecular interaction, but instead involves an additional step, consistent with
300 a conformational change in C3. Such behaviour is typical in SPR analyses where the two-state model
301 describes an initial reversible binding event, followed by a slower conformational rearrangement
302 that stabilises the complex. Taken together, these findings suggest that the interaction between C3
303 and immobilised TiO□ nanoparticles is more complex than a straightforward 1:1 binding process.
304 The estimated K_D represents the affinity for the interaction with consideration to the more complex
305 interaction.
306

307 As TiO□ nanoparticles of this size, charge and composition are leached into the bloodstream, it was
308 pertinent to investigate their physiological impact in *ex-vivo* models using red blood cells. Results
309 from the factor B binding assay showed that in the presence of TiO□, the formation of the C3

310 convertase was greatly hindered and unable to activate nearby C3. Importantly, prior biophysical
311 information showed no interaction between TiO□ and factor B, suggesting that factor B was not
312 being influenced by the nanoparticles. In combination, these data strongly indicated that the
313 interference was from an altered complement C3 protein. To assess this, we performed an
314 alternative pathway haemolysis assay to show any differences in the ability of C3 to naturally lyse
315 red blood cells in the presence of TiO_2. After 60 minutes in the absence of nanoparticle, 40 % of
316 RBCs were lysed compared to 10 % in the presence of 16 μM TiO_2, corroborating that the activity of
317 C3 was selectively reduced by the nanoparticles.
318

319 ## Structural basis for complement inhibition by titanium nanoparticles

320 We lastly sought to understand the molecular-level influence that the titanium nanoparticle
321 imparted on complement C3 and how this key protein was being inhibited. Despite its small size,
322 visualising such a metal-dense nanoparticle in the presence of proteins had evident repercussions
323 on particle alignment and 2D classification challenges.[37-39] Following a non-standard processing
324 strategy, a low-resolution reconstruction shows the interaction between C3 and a single TiO_2
325 nanoparticle. Notably, although the C3-TiO_2 data are low resolution, it is clear by the predominant
326 protein conformation that C3 indeed remains in an inactive state. The compact density produced a
327 diameter of approximately 120 Å, much more similar to the size of inactive C3 compared to
328 activated structures of 160 Å.[36] Despite the lack of a dedicated binding site for the nanoparticle,
329 the location of TiO_2 does not appear to be random as it is situated adjacent to an electropositive,
330 solvent-accessible region of the MG7 domain. In the reported C3 convertase structure (2WIN),[40] the
331 MG7 domain and C-terminal domain of C345C form a junction where factor B is able to bind (Figure
332 8). In our structure, the titanium nanoparticle is located where factor B would normally interact
333 with C3 to activate the zymogen and form the convertase, crucially, this interference at the MG7
334 domain explains why binding of factor B to C3 was inhibited, ultimately resulting in the reduction
335 of C3 convertase, C3bBb. No data suggested an equilibrium or competitive binding between TiO_2
336 and factor B to C3. This can be justified as the nanoparticle, albeit not much larger than factor B,
337 is an extremely electronegative species as the titanium core is coated by oxygen. This results in a
338 steric and electrostatic repulsive effect on the binding of factor B to C3 once TiO_2 is bound,
339 producing no interaction between the two species.

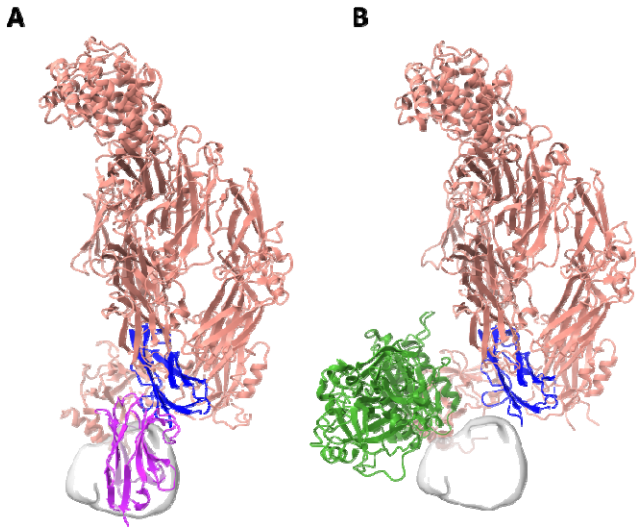

Figure 8. Two structures of C3 interacting with proteins via the MG7 domain **A)** Native C3 model (PDB 8OQ3) shown in red, MG7 domain highlighted in blue. The domain-specific nanobody (purple) is bound to the MG7 domain, inhibiting activation. The near identical location of TiO_2 density (grey) from our current structure is shown for comparison. **B)** The C3 convertase model (PDB 2WIN) shown as red, MG7 domain highlighted in blue. The proximity of the factor B (green) and TiO_2 density (grey) to MG7 show this area is vital for facilitating interactions with other regulatory complement proteins.

The MG7 domain plays a critical role in anchoring dynamic regions on the protein, such as the thioester domain, following C3 conformational changes. A recent report managed to deny the translocation of C3a and rearrangement of C3 by binding a specific nanobody to native C3.[41] To achieve this, the nanobody was found to bind at the MG7 domain in the same position as the TiO_2 nanoparticles. Therefore, the binding of the titania nanoparticles to MG7 has structural and physiological implications for the native motion of C3. The presence of the nanoparticles likely sterically hinders conformational shifts in C3, thereby locking the protein in an inactive state and disrupting intramolecular interactions necessary for the propagation of structural changes. This nanoparticle binding location demonstrates a charge complementarity between the highly electronegative, oxygen-coated, surface of the titanium nanoparticle and the charged, solvent-accessible residues on MG7. Although the resolution is not sufficient to unambiguously determine the conformation of the amino acids participating in the interaction, the location of the nanoparticle throughout all classification steps remained consistent, indicating this interaction as non-transient and stable. Importantly, no evidence from the structural or biophysical data suggests titanium nanoparticles are associated with C3 in the extended conformation or that they promote a major conformational shift to an active C3b-like state.

363

364 ## Immune system implications of titania in the blood

365 The Compstatin family of cyclic peptides are inhibitors, specific for C3, and are shown to bind in a
366 completely separate area of the protein. These inhibitor drugs are all documented to bind between
367 the MG4 and MG5 domains, approximately 60 Å away from the observed TiO_2 binding site at MG7.
368 Yet, Compstatin binding does not arrest the conformation of C3, but instead prevents cleavage by
369 convertases (C4b2a in the classical/lectin pathway and C3bBb in the alternative pathway). Large
370 nanoparticles (>100 Å) are able to generate protein coronae, activate complement and initiate MAC
371 formation in the blood. Given the biochemical and biophysical results all show a reduction in
372 complement activity, it is likely that the TiO_2 nanoparticles are recognised by the complement
373 system as a substrate inhibitor of C3, rather than as a foreign surface.[42, 43] Our findings uncover a
374 previously uncharacterised mechanism by which TiO□ nanoparticles modulate innate immune
375 responses via direct inhibition of complement component C3. Using nanoparticles that replicate the
376 physicochemical properties - size, shape, and surface charge - of those known to leach from
377 implanted medical and dental devices, we demonstrate selective suppression of the alternative
378 complement pathway. This inhibition results in reduced generation of anaphylatoxins (C3a, C5a),
379 impaired opsonisation, and decreased formation of the terminal membrane attack complex (MAC).
380 Such activity suggests that TiO□ nanoparticles may alter host immune surveillance in the context of
381 biomaterials, with implications for long-term implant biocompatibility and immune homeostasis.
382 These results expand the functional profile of TiO□ beyond its established roles in structural
383 support and surface engineering, reframing it as an active modulator of immune pathways. Our
384 observations also align with growing evidence that metal and metal oxide nanoparticles—including
385 silver, zinc oxide, cerium oxide, and gold—exert immunoregulatory effects through distinct
386 molecular targets, warranting broader investigation into nanoparticle-host interactions in clinical
387 materials.[44-46] Efforts to further elucidate these mechanisms and assess their relevance *in-vivo* are
388 ongoing in our laboratory.

389

390 # Materials and Methods

391 ## C3 isolation, purification and storage

392 Native C3 was isolated and purified in-house from human plasma according to previous reports.[47]
393 The final step of purification involved cation exchange chromatography which was performed using
394 a Mono S 5/50 GL column (GE Healthcare, Bio-Sciences AB, Uppsala, Sweden). The column was
395 equilibrated with 5 column volumes (CV) buffer A (20 mM phosphate buffer pH 6.8), followed by
396 sample application (0.25 CV). The column was washed with 3 CV of buffer A and then the elution
397 was started using a linear gradient of buffer B (20 mM phosphate buffer pH 6.8, ranging from 0 to
398 0.85M NaCl). The protein elution was monitored with an UV detector at 280 nm and fractions of 0.5
399 mL were collected during the elution procedure. C3 was precipitated in a low salt and pH buffer for
400 storage by dialysis against a 40 mM phosphate buffer with ionic strength 0.05 (mS) and pH 6.0 at
401 +4°C with a buffer volume at least 10-fold higher than the volume of C3. After 24 h the buffer was
402 replaced with fresh buffer and dialysis continued for another 24 h until a visible precipitate was
403 formed. The stock solution of precipitated native C3 was then suspended (without centrifugation)
404 and aliquoted before storage at -80°C. In order to dissolve the precipitated C3, 1-part VB^{++} (5x
405 stock solution) was added to 4-parts of precipitated C3 immediately before use.[48]
406

407 ## Preparation of sol-gel titania

408 The synthesis of the uniform titania colloids used in this work was performed by following a
409 previously reported preparation.[49] The precursor of titanium ethoxide (5 mL) was dissolved in
410 anhydrous ethanol (5 mL) followed by the addition of 1.5 mL of triethanolamine during continuous
411 stirring. A hydrolysing solution (1 mL) was produced by mixing nitric acid (0.5 M) with ethanol (2
412 mL). The resulting lightly-yellow, transparent solution contained 120 mg/mL TiO_2 according to TGA
413 measurements.[16] The obtained product was of high-enough purity to not require additional
414 purification.
415

416 ## Biophysical measurements

417 DLS, thermal unfolding and nanoDSF measurements were performed on Prometheus Panta
418 (NanoTemper, Munich, Germany) in technical triplicates. For apo-protein experiments, 0.5 mg/mL
419 of C3 in filtered MQ water or buffered solution was added to separate capillaries at room
420 temperature. For TiO_2 experiments, nanoparticles in a stock solution of 1 mM were suspended in
421 filtered MQ water, briefly incubated with C3 and added to capillaries. Immobilisation was carried

422 out using a Biacore T200 system (GE Healthcare) at 25 °C with an AU bare gold, non-derivatised
423 biosensor chip (Xantec) in Milli-Q water containing 0.05% Tween-20. A post-sonicated TiO□ solution
424 at a concentration of 1.0 µg/mL was employed for immobilisation by simple manual deposition (10
425 uL/min), exploiting the strong affinity between the gold surface and titanium oxide. The
426 immobilisation level was maintained at 300-400 RU. A reference channel was left untreated and did
427 not undergo nanoparticle immobilisation.
428 Single-cycle kinetic experiments were performed with C3 in Tris buffer (50 mM Tris-HCl, 20 mM
429 NaCl, 0.05% Tween-20, pH 7.4) under the following conditions: flow rate 75 µL/min, association
430 time 60 s, dissociation time 900 s, and C3 concentration series prepared by two-fold dilution
431 starting from 10 µM. A negative control with BSA confirmed the selectivity of the C3-TiO□
432 interaction, showing no detectable binding between BSA and the immobilised nanoparticles. Data
433 analysis was performed using the Biacore Evaluation software. All raw data were exported for
434 analysis and graph generation in GraphPad Prism version 10.0.
435

436 ## Biochemical assays

437 For capillary electrophoresis analysis by Wes immunoassay and alternative pathway haemolysis,
438 native C3 (1 µM) was preincubated with varying micromolar concentrations of TiO_2 nanoparticles in
439 VBS^{++} for 30 minutes at 37°C.
440
441 For capillary electrophoresis, 70 µg/mL of C3, C3b and C3 incubated with nanoparticles were added
442 to a preparation of Factor B (100 µg/mL) (Complement Technology Inc) and Factor D (0.5 µg/mL)
443 (Complement Technology Inc) in VBS^{++} and incubated over a time course of 5, 30 and 60 mins.
444 Individual time points were stopped with the addition of EDTA to a final concentration of 10 mM.
445 The Wes immunoassay was performed under reducing conditions with a primary mouse monoclonal
446 anti-human complement Factor Bb antibody (2 µg/mL) (Bio-Rad Laboratories).
447
448 The alternative pathway haemolysis assay was set up and adapted according to previous methods,[50,
449 51] where 25 µL of C3 (200 µg/mL) preincubated with 0.5, 1, 2, 4, 8 and 16 µM of TiO_2 nanoparticles
450 were added to 50 µL C3 depleted serum (Complement Technology Inc) followed by the addition of
451 100 µL 50% rabbit erythrocytes (v/v) in GVB Mg EGTA. These samples were then incubated in a

452 shaking water bath for 20 mins at 37°C at 200 rpm before being stopped with the addition of cold
453 VB-EDTA. The samples were then centrifuged at 860 g for 10 mins at 4°C and absorbance measured
454 at 540 nm on a CLARIOstar Plus (BMG Labtech).
455
456

457 ## Cryo-EM structure determination of native C3

458 C3 protein buffer was exchanged from VB^{++} to filtered MQ water and concentrated to 0.4 mg/mL
459 before grid freezing. Cryo-EM samples were prepared on UltrAuFoil R1.2/1.3 300 mesh holey gold
460 grids (Quantifoil Microtools). Once the grids were glow discharged with a PELCO easiGlow
461 instrument (20 mA, 0.4 mBar, 1.5 min), 3 μL of C3 was applied to the glow-discharged grids.
462 Vitrification was performed with a Vitrobot Mark IV (Thermo Fisher Scientific) at 4 °C and 95 %
463 humidity. Grids were blotted in duplicate for 3 seconds and plunged into liquid ethane. Following
464 vitrification, the grids were clipped into autogrid cartridges (Thermo Fisher Scientific) for use with
465 autoloader systems.
466
467 All grids were ATLAS screened on a Glacios 200 kV cryo-electron microscope mounted with a Falcon
468 III direct electron detector. Data were acquired in EER format at a pixel size of 0.7463 Å/pixel with
469 a dose rate of 0.91 electrons $pixel^{-1}$ sec^{-1}. Approximately 1200 micrographs had 2x binning applied
470 and were processed using exposures fractionated into 50 frames for motion correction. This
471 enabled for a rapid assessment of the sample quality, particle density and distribution before high-
472 resolution data were collected. For full data collections, a 300 kV Titan Krios G2 (Thermo Scientific)
473 transmission electron microscope equipped with a K3 detector (Gatan) and a 20 eV BioQuantum
474 energy filter (Gatan), was used. Data were collected with the following settings: 0.648 Å/pixel (190
475 kx magnification), 51 $e^{-}/Å^2$ total electron dose, −0.5 to −2.5 µm defocus range. Automated
476 collection was performed using the EPU software (Thermo Scientific) with 30° stage tilting. A total
477 of 17,420 movies were collected.
478
479 During data collection, cryoSPARC live (cryoSPARC v4.1.1) was employed for on-the-fly data
480 processing for the first few hundred micrographs using the same settings as for the initial screening
481 dataset. Processing was performed in cryoSPARC v4.6.0[52] and included initial Patch Motion

482 Correction and Patch CTF being performed before micrograph curation. Micrographs were manually
483 curated based on CFT estimations, total frame motion, defocus, ice thickness and contamination.
484 Using the obtained template from the screening dataset, all particle picking was performed with
485 template picker and the Topaz[53] wrapper template picker in cryoSPARC. Once data collection was
486 completed, the template-based picks totalled ~5 million and were 2x downsampled and extracted
487 with a 400 x 400 box size before being Fourier-cropped to 250 x 250 pixels. Particles were classified
488 into 150 2D classes (10 Å minimum separation distance, 170 - 200 Å circular mask inner-diameter, 2
489 final full iterations, 40 online-EM iterations, 400 batch size per class). Following 2D class selection,
490 this classification/selection procedure was repeated twice more which resulted in ~1.9 million
491 particles suitable for *Ab-initio* reconstruction. *Ab-initio* reconstruction was followed by
492 heterogenous refinement using a few poor density "dummy" classes as seeds for junk particles. Two
493 further rounds of heterogenous refinement seeding resulted in 818,343 particles which displayed
494 discrete heterogeneity, which was elucidated using 3D variability analysis.[54] Masked refinement and
495 reconstruction jobs reliably produced densities at resolutions of ~2.5 Å. 3D variability analysis
496 demonstrated the inherent continuous disorder of the particles and was used to separate individual
497 latent dimensions of motion attributed to approximately 3 states experienced by the particles.
498 Particles responsible for each state were isolated and reconstructed independently to produce each
499 individual C3 pose.
500
501 A model was constructed by using the reported inactive C3 structure (PDB 2A73)[36] as a starting
502 model. Owing to the large conformational differences between the current particles and the
503 reported structure, the domains were individually docked and fitted into the electron density with
504 UCSF ChimeraX version 1.9.[55] These hand-fitted domains were then quantitatively fitted into the
505 density and refined using the DockEM[56] and Refmac Servalcat[57] packages within CCP-EM 1.6.0.[58] The
506 Coot[59] program was used for manual rebuilding and inspection of the model in the electron density
507 before a final real-space refinement run in PHENIX.[60] The relevant structural validation metrics are
508 shown in supplementary Table 1.
509
510 Cryo-EM structure determination of C3-TiO_2

511 As previous, C3 protein buffer was exchanged from VB^{++} to filtered MQ water and concentrated to
512 0.4 mg/mL before grid freezing. Cryo-EM samples were prepared on UltrAuFoil R1.2/1.3 300 mesh
513 holey gold grids (Quantifoil Microtools). While the grids were glow discharged with a PELCO
514 easiGlow instrument (20 mA, 0.4 mBar, 1.5 min), C3 was incubated with nanoparticles at an
515 equimolar concentration for 5 minutes on ice before 3 μL of the mixture was applied to the glow-
516 discharged grids. Vitrification was performed with a Vitrobot Mark IV (Thermo Fisher Scientific) at 4
517 °C and 95 % humidity. Grids were blotted in duplicate for 3 seconds and plunged into liquid ethane.
518 Following vitrification, the grids were clipped into autogrid cartridges (Thermo Fisher Scientific) for
519 use with autoloader systems.
520
521 A 300 kV Titan Krios G2 (Thermo Scientific) transmission electron microscope equipped with a K3
522 detector (Gatan) and a 20 eV BioQuantum energy filter (Gatan), was used for the full data
523 collections. Data were collected with the following settings: 0.648 Å/pixel (190 kx magnification),
524 51 $e^-/Å^2$ total electron dose, −0.5 to −2.5 μm defocus range. Automated collection was performed
525 using the EPU software (Thermo Scientific) and a total of 17,706 movies were collected. Processing
526 was performed in cryoSPARC v4.6.0 and included initial Patch Motion Correction and Patch CTF
527 being performed before micrograph curation. Micrographs were manually curated based on CFT
528 estimations, total frame motion, defocus, ice thickness and contamination.
529
530 A visual inspection of the micrographs and blob-picked classes in cryoSPARC suggested there was a
531 clear picking bias which made further classification and alignment impossible (ESI Figure S4a). As
532 the electron dosage charged the TiO_2, the nanoparticles appeared as bright hotspots on the
533 micrographs which almost completely overpowered signals attributed to protein. Attempts to use
534 the previous C3 reconstruction as a picking template were unsuccessful due to the picking
535 algorithm being unable to locate any signal related to protein. Analysis of the protein and TiO_2
536 relative intensities in EMAN2[61] showed that there was approximately a 1:10 intensity disparity
537 between the protein and nanoparticles, respectively (ESI Figure S4c). Attempts to enforce non-
538 negativity, solvent-clamping and template picking using native C3 prior to 2D classification proved
539 unsuccessful as the picking was strongly biased toward the most intense signals of the
540 nanoparticles. To the best of our knowledge, cryoSPARC does not have the ability for the user to

541 manually threshold and normalise intensities, and for this reason we attempted to complete the
542 data processing using RELION 5.0.[62] Following a standard pre-processing strategy up to CTF
543 estimation, Topaz was trained on a small subset of particles and once training converged, particles
544 were extracted from all micrographs. The extraction job settings were not default: particle box
545 size 384 pixels, diameter background circle 40 pixels, stddev white dust removal -1.0, stddev black
546 dust removal 3.0, with normalisation on and a minimum FOM of 1.0. The relion image handler tool
547 was used to threshold a series of incremental values from 1.0 – 3.0 in order to find which cutoff
548 yielded the best SNR of both protein and nanoparticle. After 2D classification was run on each
549 thresholded particle stack, normalisation was run using the relion stack create and relion
550 preprocess tools. Performing this step was found to improve particle alignment as well as provide
551 an intensity distribution favoured by RELION. A low-resolution map was obtained from the
552 thresholded and normalised particle stack after running through 2D classification, 3D reconstruction
553 and masked refinement.
554
555 The obtained density showed most domains present excluding those in the macroglobulin head
556 region (MG1-4). Excluding this missing area, the domains were individually docked and fitted into
557 the electron density with UCSF ChimeraX version 1.9, which conformed to the inactive state C3
558 conformation.
559

560 Structural and statistical image preparation

561 All cryo-EM images were prepared using ChimeraX. All biophysical and biochemical graphs and
562 analyses have been prepared, fitted and displayed using the program GraphPad Prism version 10.0.
563

564 Acknowledgements and funding

565 We gratefully acknowledge the Cryo-EM Uppsala facility for the use of the Glacios microscope,
566 computational facilities and the expert technical support of Daniel Larsson, all of which is funded
567 by the Department of Cell and Molecular Biology, the Disciplinary Domains of Science and
568 Technology and of Medicine and Pharmacy at Uppsala University. This work was supported by the
569 SciLifeLab & Wallenberg Data Driven Life Science Program, Knut and Alice Wallenberg
570 Foundation (grants: KAW 2020.0239 and KAW 2017.0003), and by the National Bioinformatics

Infrastructure Sweden (NBIS) at SciLifeLab. We would like to especially thank Dustin Morado, Tim Schulte, Piotr Draczkowski and Helena Danielson for their expert assistance with data collection and interpretation. The computations and data handling were additionally enabled by resources provided by the National Academic Infrastructure for Supercomputing in Sweden (NAISS), partially funded by the Swedish Research Council through grant agreement no. 2022-06725. This work was supported by the Swedish research council grant number 2022-03971_VR. We kindly thank Guillermo Pérez Ropero and Ridgeview Instruments AB for the C1 SPR sensor chip donation.

Author contributions

M.S, K.N.E, B.N and V.G.K conceptualised the research. G.A.S synthesised the pure titania colloidal nanoparticles. J.W performed SPR, data analysis and generated the figures and text. D.E and K.F purified the C3 protein and performed all biochemical and haemolysis assays. J.J.W performed DLS and nanoDSF characterisations with C3 and TiO_2. J.J.W prepared all TEM grids, performed data collection, processing, model refinement and validation of all cryo-EM structures. J.J.W and D.E compiled and analysed the data, wrote the original manuscript and prepared figures and tables. Editorial assistance was provided by V.G.K, G.A.S, M.S, B.N and K.N.E. All authors have reviewed, edited and approved the final version of the manuscript.

Competing interests

The authors declare no conflicts of interest.

Data availability

Original data points are shown in the manuscript. Additional information can be obtained from the corresponding author upon request.

References

1. Zhang, C.; Derrien, M.; Levenez, F.; Brazeilles, R.; Ballal, S. A.; Kim, J.; Degivry, M. C.; Quere, G.; Garault, P.; van Hylckama Vlieg, J. E.; et al. Ecological robustness of the gut microbiota in

response to ingestion of transient food-borne microbes. *ISME J* **2016**, *10* (9), 2235-2245. DOI: 10.1038/ismej.2016.13.

2. Sadeghi, R.; Rodriguez, R. J.; Yao, Y.; Kokini, J. L. Advances in Nanotechnology as They Pertain to Food and Agriculture: Benefits and Risks. *Annu Rev Food Sci Technol* **2017**, *8*, 467-492. DOI: 10.1146/annurev-food-041715-033338.

3. Baranowska-Wojcik, E. Factors Conditioning the Potential Effects TiO2 NPs Exposure on Human Microbiota: a Mini-Review. *Biol Trace Elem Res* **2021**, *199* (12), 4458-4465. DOI: 10.1007/s12011-021-02578-5.

4. Baranowska-Wojcik, E.; Szwajgier, D.; Oleszczuk, P.; Winiarska-Mieczan, A. Effects of Titanium Dioxide Nanoparticles Exposure on Human Health-a Review. *Biol Trace Elem Res* **2020**, *193* (1), 118-129. DOI: 10.1007/s12011-019-01706-6.

5. Liao, F.; Chen, L.; Liu, Y.; Zhao, D.; Peng, W.; Wang, W.; Feng, S. The size-dependent genotoxic potentials of titanium dioxide nanoparticles to endothelial cells. *Environ Toxicol* **2019**, *34* (11), 1199-1207. DOI: 10.1002/tox.22821.

6. Chouirfa, H.; Bouloussa, H.; Migonney, V.; Falentin-Daudre, C. Review of titanium surface modification techniques and coatings for antibacterial applications. *Acta Biomater* **2019**, *83*, 37-54. DOI: 10.1016/j.actbio.2018.10.036.

7. Seisenbaeva, G. A.; Daniel, G.; Nedelec, J. M.; Kessler, V. G. Solution equilibrium behind the room-temperature synthesis of nanocrystalline titanium dioxide. *Nanoscale* **2013**, *5* (8), 3330-3336. DOI: 10.1039/c3nr34068f.

8. Mudunkotuwa, I. A.; Grassian, V. H. Citric acid adsorption on TiO2 nanoparticles in aqueous suspensions at acidic and circumneutral pH: surface coverage, surface speciation, and its impact on nanoparticle-nanoparticle interactions. *J Am Chem Soc* **2010**, *132* (42), 14986-14994. DOI: 10.1021/ja106091q.

9. Shim, K. H.; Hulme, J.; Maeng, E. H.; Kim, M. K.; An, S. S. Analysis of zinc oxide nanoparticles binding proteins in rat blood and brain homogenate. *Int J Nanomedicine* **2014**, *9 Suppl 2* (Suppl 2), 217-224. DOI: 10.2147/IJN.S58204.

10. Brun, E.; Carriere, M.; Mabondzo, A. In vitro evidence of dysregulation of blood-brain barrier function after acute and repeated/long-term exposure to TiO(2) nanoparticles. *Biomaterials* **2012**, *33* (3), 886-896. DOI: 10.1016/j.biomaterials.2011.10.025.

11. Liu, X.; Sui, B.; Sun, J. Size- and shape-dependent effects of titanium dioxide nanoparticles on the permeabilization of the blood-brain barrier. *J Mater Chem B* **2017**, *5* (48), 9558-9570. DOI: 10.1039/c7tb01314k.

12. Shemetov, A. A.; Nabiev, I.; Sukhanova, A. Molecular interaction of proteins and peptides with nanoparticles. *ACS Nano* **2012**, *6* (6), 4585-4602. DOI: 10.1021/nn300415x.

13. Saptarshi, S. R.; Duschl, A.; Lopata, A. L. Interaction of nanoparticles with proteins: relation to bio-reactivity of the nanoparticle. *J Nanobiotechnology* **2013**, *11*, 26. DOI: 10.1186/1477-3155-11-26.

14. Li, J. J.; Zou, L.; Hartono, D.; Ong, C. N.; Bay, B. H.; Lanry Yung, L. Y. Gold Nanoparticles Induce Oxidative Damage in Lung Fibroblasts In Vitro. *Advanced Materials* **2007**, *20* (1), 138-142. DOI: 10.1002/adma.200701853.

15. Monopoli, M. P.; Aberg, C.; Salvati, A.; Dawson, K. A. Biomolecular coronas provide the biological identity of nanosized materials. *Nat Nanotechnol* **2012**, *7* (12), 779-786. DOI: 10.1038/nnano.2012.207.

16. Seisenbaeva, G. A.; Fromell, K.; Vinogradov, V. V.; Terekhov, A. N.; Pakhomov, A. V.; Nilsson, B.; Ekdahl, K. N.; Vinogradov, V. V.; Kessler, V. G. Dispersion of TiO(2) nanoparticles improves burn wound healing and tissue regeneration through specific interaction with blood serum proteins. *Sci Rep* **2017**, *7* (1), 15448. DOI: 10.1038/s41598-017-15792-w.

17. Ekdahl, K. N.; Teramura, Y.; Hamad, O. A.; Asif, S.; Duehrkop, C.; Fromell, K.; Gustafson, E.; Hong, J.; Kozarcanin, H.; Magnusson, P. U.; et al. Dangerous liaisons: complement, coagulation, and kallikrein/kinin cross-talk act as a linchpin in the events leading to thromboinflammation. *Immunol Rev* **2016**, *274* (1), 245-269. DOI: 10.1111/imr.12471.

18. Eriksson, O.; Mohlin, C.; Nilsson, B.; Ekdahl, K. N. The Human Platelet as an Innate Immune Cell: Interactions Between Activated Platelets and the Complement System. *Front Immunol* **2019**, *10*, 1590. DOI: 10.3389/fimmu.2019.01590.

19. Nesargikar, P. N.; Spiller, B.; Chavez, R. The complement system: history, pathways, cascade and inhibitors. *Eur J Microbiol Immunol (Bp)* **2012**, *2* (2), 103-111.

20. Ricklin, D.; Hajishengallis, G.; Yang, K.; Lambris, J. D. Complement: a key system for immune surveillance and homeostasis. *Nat Immunol* **2010**, *11* (9), 785-797. DOI: 10.1038/ni.1923.

21. Wang, Z.; Hood, E. D.; Nong, J.; Ding, J.; Marcos-Contreras, O. A.; Glassman, P. M.; Rubey, K. M.; Zaleski, M.; Espy, C. L.; Gullipali, D.; et al. Combating Complement's Deleterious Effects on Nanomedicine by Conjugating Complement Regulatory Proteins to Nanoparticles. *Adv Mater* **2022**, *34* (8), e2107070. DOI: 10.1002/adma.202107070.

22. Merle, N. S.; Church, S. E.; Fremeaux-Bacchi, V.; Roumenina, L. T. Complement System Part I - Molecular Mechanisms of Activation and Regulation. *Front Immunol* **2015**, *6*, 262. DOI: 10.3389/fimmu.2015.00262.

23. Zarantonello, A.; Revel, M.; Grunenwald, A.; Roumenina, L. T. C3-dependent effector functions of complement. *Immunol Rev* **2023**, *313* (1), 120-138. DOI: 10.1111/imr.13147.

24. Tack, B. F.; Harrison, R. A.; Janatova, J.; Thomas, M. L.; Prahl, J. W. Evidence for presence of an internal thiolester bond in third component of human complement. *Proc Natl Acad Sci U S A* **1980**, *77* (10), 5764-5768. DOI: 10.1073/pnas.77.10.5764.

25. Gros, P.; Milder, F. J.; Janssen, B. J. Complement driven by conformational changes. *Nat Rev Immunol* **2008**, *8* (1), 48-58. DOI: 10.1038/nri2231.

26. Markiewski, M. M.; Nilsson, B.; Ekdahl, K. N.; Mollnes, T. E.; Lambris, J. D. Complement and coagulation: strangers or partners in crime? *Trends Immunol* **2007**, *28* (4), 184-192. DOI: 10.1016/j.it.2007.02.006.

27. Ricklin, D.; Reis, E. S.; Mastellos, D. C.; Gros, P.; Lambris, J. D. Complement component C3 - The "Swiss Army Knife" of innate immunity and host defense. *Immunol Rev* **2016**, *274* (1), 33-58. DOI: 10.1111/imr.12500.

28. Sfyroera, G.; Ricklin, D.; Reis, E. S.; Chen, H.; Wu, E. L.; Kaznessis, Y. N.; Ekdahl, K. N.; Nilsson, B.; Lambris, J. D. Rare loss-of-function mutation in complement component C3 provides insight into molecular and pathophysiological determinants of complement activity. *J Immunol* **2015**, *194* (7), 3305-3316. DOI: 10.4049/jimmunol.1402781.

29. E, S. R.; Falcao, D. A.; Isaac, L. Clinical aspects and molecular basis of primary deficiencies of complement component C3 and its regulatory proteins factor I and factor H. *Scand J Immunol* **2006**, *63* (3), 155-168. DOI: 10.1111/j.1365-3083.2006.01729.x.

30. Nilsson, U. R.; Nilsson, B.; Storm, K. E.; Sjolin-Forsberg, G.; Hallgren, R. Hereditary dysfunction of the third component of complement associated with a systemic lupus erythematosus-like syndrome and meningococcal meningitis. *Arthritis Rheum* **1992**, *35* (5), 580-586. DOI: 10.1002/art.1780350516.

31. Qu, H.; Magotti, P.; Ricklin, D.; Wu, E. L.; Kourtzelis, I.; Wu, Y. Q.; Kaznessis, Y. N.; Lambris, J. D. Novel analogues of the therapeutic complement inhibitor compstatin with significantly improved affinity and potency. *Mol Immunol* **2011**, *48* (4), 481-489. DOI: 10.1016/j.molimm.2010.10.004.

32. Sahu, A.; Soulika, A. M.; Morikis, D.; Spruce, L.; Moore, W. T.; Lambris, J. D. Binding kinetics, structure-activity relationship, and biotransformation of the complement inhibitor compstatin. *J Immunol* **2000**, *165* (5), 2491-2499. DOI: 10.4049/jimmunol.165.5.2491.

33. Janssen, B. J.; Gros, P. Structural insights into the central complement component C3. *Mol Immunol* **2007**, *44* (1-3), 3-10. DOI: 10.1016/j.molimm.2006.06.017.

34. Nishida, N.; Walz, T.; Springer, T. A. Structural transitions of complement component C3 and its activation products. *Proc Natl Acad Sci U S A* **2006**, *103* (52), 19737-19742. DOI: 10.1073/pnas.0609791104.

35. FitzGerald, E. A.; Cederfelt, D.; Kovryzhenko, D.; Boronat, P.; Lund, B. A.; Dobritzsch, D.; Hennig, S.; Paseiro, P. P.; de Esch, I.; Danielson, U. H. Detection and characterisation of ligand-induced conformational changes in acetylcholine binding proteins using biosensors and X-ray crystallography. *RSC Chemical Biology* **2025**. DOI: 10.1039/d5cb00041f.

36. Janssen, B. J.; Huizinga, E. G.; Raaijmakers, H. C.; Roos, A.; Daha, M. R.; Nilsson-Ekdahl, K.; Nilsson, B.; Gros, P. Structures of complement component C3 provide insights into the function and evolution of immunity. *Nature* **2005**, *437* (7058), 505-511. DOI: 10.1038/nature04005.

37. Yu, G.; Yan, R.; Zhang, C.; Mao, C.; Jiang, W. Single-Particle Cryo-EM and 3D Reconstruction of Hybrid Nanoparticles with Electron-Dense Components. *Small* **2015**, *11* (38), 5157-5163. DOI: 10.1002/smll.201500531.

38. Montesano-Roditis, L.; Glitz, D. G.; Traut, R. R.; Stewart, P. L. Cryo-electron microscopic localization of protein L7/L12 within the Escherichia coli 70 S ribosome by difference mapping and Nanogold labeling. *J Biol Chem* **2001**, *276* (17), 14117-14123. DOI: 10.1074/jbc.M008430200.

39. Chen, C.; Daniel, M. C.; Quinkert, Z. T.; De, M.; Stein, B.; Bowman, V. D.; Chipman, P. R.; Rotello, V. M.; Kao, C. C.; Dragnea, B. Nanoparticle-templated assembly of viral protein cages. *Nano Lett* **2006**, *6* (4), 611-615. DOI: 10.1021/nl0600878.

40. Rooijakkers, S. H.; Wu, J.; Ruyken, M.; van Domselaar, R.; Planken, K. L.; Tzekou, A.; Ricklin, D.; Lambris, J. D.; Janssen, B. J.; van Strijp, J. A.; et al. Structural and functional implications of the alternative complement pathway C3 convertase stabilized by a staphylococcal inhibitor. *Nat Immunol* **2009**, *10* (7), 721-727. DOI: 10.1038/ni.1756.

41. Gadeberg, T. A. F.; Jorgensen, M. H.; Olesen, H. G.; Lorentzen, J.; Harwood, S. L.; Almeida, A. V.; Fruergaard, M. U.; Jensen, R. K.; Kanis, P.; Pedersen, H.; et al. Cryo-EM analysis of complement C3 reveals a reversible major opening of the macroglobulin ring. *Nat Struct Mol Biol* **2025**, *32* (5), 884-895. DOI: 10.1038/s41594-024-01467-4.

42. Pangburn, M. K.; Morrison, D. C.; Schreiber, R. D.; Müller-Eberhard, H. J. Activation of the alternative complement pathway: recognition of surface structures on activators by bound C3b. *The Journal of Immunology* **1980**, *124* (2), 977-982. DOI: 10.4049/jimmunol.124.2.977.

43. Bajic, G.; Yatime, L.; Sim, R. B.; Vorup-Jensen, T.; Andersen, G. R. Structural insight on the recognition of surface-bound opsonins by the integrin I domain of complement receptor 3. *Proc Natl Acad Sci U S A* **2013**, *110* (41), 16426-16431. DOI: 10.1073/pnas.1311261110.

44. Moyano, D. F.; Liu, Y.; Ayaz, F.; Hou, S.; Puangploy, P.; Duncan, B.; Osborne, B. A.; Rotello, V. M. Immunomodulatory effects of coated gold nanoparticles in LPS-stimulated in vitro and in vivo murine model systems. *Chem* **2016**, *1* (2), 320-327. DOI: 10.1016/j.chempr.2016.07.007.

45. Hirst, S. M.; Karakoti, A. S.; Tyler, R. D.; Sriranganathan, N.; Seal, S.; Reilly, C. M. Anti-inflammatory properties of cerium oxide nanoparticles. *Small* **2009**, *5* (24), 2848-2856. DOI: 10.1002/smll.200901048.

46. Poon, W. L.; Alenius, H.; Ndika, J.; Fortino, V.; Kolhinen, V.; Mesceriakovas, A.; Wang, M.; Greco, D.; Lahde, A.; Jokiniemi, J.; et al. Nano-sized zinc oxide and silver, but not titanium dioxide, induce innate and adaptive immunity and antiviral response in differentiated THP-1 cells. *Nanotoxicology* **2017**, *11* (7), 936-951. DOI: 10.1080/17435390.2017.1382600.

47. Hammer, C. H.; Wirtz, G. H.; Renfer, L.; Gresham, H. D.; Tack, B. F. Large scale isolation of functionally active components of the human complement system. *Journal of Biological Chemistry* **1981**, *256* (8), 3995-4006. DOI: 10.1016/s0021-9258(19)69557-8.

48. Adler, A.; Manivel, V. A.; Fromell, K.; Teramura, Y.; Ekdahl, K. N.; Nilsson, B. A Robust Method to Store Complement C3 With Superior Ability to Maintain the Native Structure and Function of the Protein. *Front Immunol* **2022**, *13*, 891994. DOI: 10.3389/fimmu.2022.891994.

49. Kessler, V. G.; Seisenbaeva, G. A.; Unell, M.; Hakansson, S. Chemically triggered biodelivery using metal-organic sol-gel synthesis. *Angew Chem Int Ed Engl* **2008**, *47* (44), 8506-8509. DOI: 10.1002/anie.200803307.

50. Fromell, K.; Adler, A.; Aman, A.; Manivel, V. A.; Huang, S.; Duhrkop, C.; Sandholm, K.; Ekdahl, K. N.; Nilsson, B. Assessment of the Role of C3(H(2)O) in the Alternative Pathway. *Front Immunol* **2020**, *11*, 530. DOI: 10.3389/fimmu.2020.00530.

51. Nilsson, U. R.; Nilsson, B. Simplified assays of hemolytic activity of the classical and alternative complement pathways. *J Immunol Methods* **1984**, *72* (1), 49-59. DOI: 10.1016/0022-1759(84)90432-0.

52. Punjani, A.; Rubinstein, J. L.; Fleet, D. J.; Brubaker, M. A. cryoSPARC: algorithms for rapid unsupervised cryo-EM structure determination. *Nat Methods* **2017**, *14* (3), 290-296. DOI: 10.1038/nmeth.4169.

53. Bepler, T.; Morin, A.; Rapp, M.; Brasch, J.; Shapiro, L.; Noble, A. J.; Berger, B. Positive-unlabeled convolutional neural networks for particle picking in cryo-electron micrographs. *Nat Methods* **2019**, *16* (11), 1153-1160. DOI: 10.1038/s41592-019-0575-8.

54. Punjani, A.; Fleet, D. J. 3D variability analysis: Resolving continuous flexibility and discrete heterogeneity from single particle cryo-EM. *J Struct Biol* **2021**, *213* (2), 107702. DOI: 10.1016/j.jsb.2021.107702.

55. Meng, E. C.; Goddard, T. D.; Pettersen, E. F.; Couch, G. S.; Pearson, Z. J.; Morris, J. H.; Ferrin, T. E. UCSF ChimeraX: Tools for structure building and analysis. *Protein Sci* **2023**, *32* (11), e4792. DOI: 10.1002/pro.4792.

56. Zou, J.; Zhang, W.; Hu, J.; Zhou, X.; Zhang, B. DockEM: an enhanced method for atomic-scale protein-ligand docking refinement leveraging low-to-medium resolution cryo-EM density maps. *Brief Bioinform* **2025**, *26* (2). DOI: 10.1093/bib/bbaf091.

57. Yamashita, K.; Palmer, C. M.; Burnley, T.; Murshudov, G. N. Cryo-EM single-particle structure refinement and map calculation using Servalcat. *Acta Crystallogr D Struct Biol* **2021**, *77* (Pt 10), 1282-1291. DOI: 10.1107/S2059798321009475.

58. Wood, C.; Burnley, T.; Patwardhan, A.; Scheres, S.; Topf, M.; Roseman, A.; Winn, M. Collaborative computational project for electron cryo-microscopy. *Acta Crystallogr D Biol Crystallogr* **2015**, *71* (Pt 1), 123-126. DOI: 10.1107/S1399004714018070.

59. Emsley, P.; Cowtan, K. Coot: model-building tools for molecular graphics. *Acta Crystallogr D Biol Crystallogr* **2004**, *60* (Pt 12 Pt 1), 2126-2132. DOI: 10.1107/S0907444904019158.

60. Afonine, P. V.; Poon, B. K.; Read, R. J.; Sobolev, O. V.; Terwilliger, T. C.; Urzhumtsev, A.; Adams, P. D. Real-space refinement in PHENIX for cryo-EM and crystallography. *Acta Crystallogr D Struct Biol* **2018**, *74* (Pt 6), 531-544. DOI: 10.1107/S2059798318006551.

61. Tang, G.; Peng, L.; Baldwin, P. R.; Mann, D. S.; Jiang, W.; Rees, I.; Ludtke, S. J. EMAN2: an extensible image processing suite for electron microscopy. *J Struct Biol* **2007**, *157* (1), 38-46. DOI: 10.1016/j.jsb.2006.05.009.

62. Kimanius, D.; Dong, L.; Sharov, G.; Nakane, T.; Scheres, S. H. W. New tools for automated cryo-EM single-particle analysis in RELION-4.0. *Biochem J* **2021**, *478* (24), 4169-4185. DOI: 10.1042/BCJ20210708.